

TESTING ASTRO-H MEASUREMENTS OF BULK AND TURBULENT GAS MOTIONS IN GALAXY CLUSTERS

NAOMI OTA¹, DAISUKE NAGAI^{2,3}, AND ERWIN T. LAU^{2,3}

¹Department of Physics, Nara Women's University, Kitaoyanishi-machi, Nara, Nara 630-8506, Japan; naomi@cc.nara-wu.ac.jp

²Department of Physics, Yale University, New Haven, CT 06520, USA

³Yale Center for Astronomy and Astrophysics, Yale University, New Haven, CT 06520, USA

Draft version July 13, 2015

ABSTRACT

Gas motions in galaxy clusters play important roles in determining the properties of the intracluster medium (ICM) and constraining cosmological parameters using X-ray and Sunyaev-Zel'dovich effect observations of galaxy clusters. The upcoming ASTRO-H mission, equipped with high-resolution X-ray spectrometer, will make the first direct measurements of gas motions in galaxy clusters through measurements of Doppler shifting and broadening of emission lines. However, the physical interpretation of the data will be challenging due to the complex thermal and velocity structures of the ICM. In this work, we investigate how well we can measure bulk and turbulent gas motions in the ICM with ASTRO-H, by analyzing mock ASTRO-H simulations of galaxy clusters extracted from cosmological hydrodynamic simulations. We assess how photon counts, spectral fitting methods, multiphase ICM structure, deprojections, and region selection affect the measurements of gas motions. We show that while ASTRO-H is capable of recovering the underlying spherically averaged velocity profiles to within 20% with reasonable amount of photon counts ($\gtrsim 200$) in the 6.7 keV Fe XXV line complex, there are considerable azimuthal variations in the ICM velocities, even in dynamically relaxed systems, which must be taken into account when interpreting data and developing observing strategies. Finally, we show that ASTRO-H should enable direct measurements of the hydrostatic mass bias with an accuracy of $\lesssim 5\%$, by accounting for both rotational and random velocities from Doppler shifts and broadening of emission lines. Our results are broadly applicable for future X-ray missions, such as *Athena+* and *SMART-X*.

Subject headings: cosmology: theory – galaxies: clusters: general – methods: numerical – X-rays: galaxies: clusters

1. INTRODUCTION

In the hierarchical structure formation scenario, galaxy clusters are believed to grow through mergers and continuous mass accretion through the cosmic-web of large-scale structures. These mergers and accretion events stir up the hot gas in the deep gravitational potential well of the cluster, generating large-scale motions (Vazza et al. 2009, 2011; Miniati 2015). Non-thermal pressure provided by these internal gas motions exerts an extra non-thermal pressure support to the intracluster medium (ICM) (Lau et al. 2009; Battaglia et al. 2012; Nelson et al. 2014; Shi & Komatsu 2014; Shi et al. 2015), introduces bias in the hydrostatic mass estimates of galaxy clusters (e.g., Rasia et al. 2006; Nagai et al. 2007b; Nelson et al. 2012; Ettori et al. 2013), and serves as one of the primary sources of systematic uncertainties in cluster-based cosmological constraints (e.g., Allen et al. 2008; Vikhlinin et al. 2009; Planck Collaboration 2015). However, the nature of gas motions in galaxy clusters are still poorly understood. While there are indirect constraints on the level of gas motions through spatial fluctuations in thermal pressure (Schuecker et al. 2004) and X-ray surface brightness (Churazov et al. 2012), direct observational constraints from emission lines are still missing, and only upper limits are available (Ota et al. 2007; Tamura et al. 2011; Sanders & Fabian 2013).

The upcoming ASTRO-H X-ray mission (Takahashi et al. 2014), equipped with high energy resolution (~ 5 eV) Soft X-ray Spectrometer (SXS) (Mitsuda et al. 2014), will make the first direct measurement of bulk and turbulent gas motions, through shifting and broadening of the 6.7 keV Fe XXV $K\alpha$ line. These measurements will provide new insights into the physics of energy feedback from active galactic nuclei

(AGN), dynamics of cluster mergers, and chemical enrichment of the ICM (Kitayama et al. 2014). However, since the thermal and velocity structures of the ICM are rich and complex, interpretation of upcoming ASTRO-H measurements requires detailed cosmological simulations that include all relevant astrophysical processes.

As the first measurements of ICM velocities are expected soon, there are several questions that must be addressed before we can analyze and interpret the ASTRO-H data in a meaningful way. How well can ASTRO-H measure and separate bulk and turbulent motions in clusters? What are optimal observing and analysis strategies? Can we use ASTRO-H to measure the non-thermal pressure in the ICM and correct for the hydrostatic mass bias of galaxy clusters?

The primary goal of this work is to address these questions by analyzing mock ASTRO-H observations of galaxy clusters extracted from high-resolution hydrodynamical cosmological simulations. These simulations capture internal motions in the ICM generated by mergers and accretion events in the hierarchical structure formation model. We create a realistic mock ASTRO-H data of simulated clusters, analyze them using the data analysis pipeline used to analyze real X-ray data, and compare derived velocity measurements to “true” values measured directly in the simulations. We find that the spherically mass-weighted averaged ICM temperature and velocity profiles can be measured with the accuracy of better than 20%, which leads to good recovery of the hydrostatic mass bias to 5%, provided that there are at least 200 photons in the 6.7 keV Fe XXV $K\alpha$ line. However, our results also reveal considerable azimuthal variations in both bulk and turbulent velocities in the ICM (by up to factors of 2) at a given radius

even for dynamically relaxed looking clusters. We discuss implications of these azimuthal variations in correcting the hydrostatic mass bias using ASTRO-H cluster observations.

This paper is organized as follows. Section 2 describes numerical simulations and mock ASTRO-H simulations used in this work. Results are presented in Section 3. We present discussion and conclusions in Section 4 and 5, respectively.

2. SIMULATIONS

2.1. Hydrodynamical Simulations

The simulations presented in this work are performed using the Adaptive Refinement Tree (ART) N -body+gas-dynamics code (Kravtsov 1999; Kravtsov et al. 2002; Rudd et al. 2008), which is an Eulerian code that uses adaptive refinement in space and time, and non-adaptive refinement in mass (Klypin et al. 2001) to achieve the dynamic ranges necessary to resolve the cores of halos formed in self-consistent cosmological simulations. The code is parallelized using Message Passing Interface (MPI) libraries and OpenMP directives.

We analyzed a sample of high-resolution hydrodynamical simulations of galaxy clusters formation from Nagai et al. (2007a,b, hereafter N07), performed with non-radiative gas physics. Likely targets for ASTRO-H would be nearby X-ray luminous massive clusters. Thus, we focus on two X-ray luminous clusters, CL104 and CL101, at $z = 0$, with the core-excised X-ray temperature of $T_X = 7.7$ and 8.7 keV, respectively. Each cluster is simulated using a 128^3 uniform grid with 8 levels of refinement. Clusters are selected from $120h^{-1}$ Mpc computational boxes, achieving peak spatial resolution of $\approx 3.6h^{-1}$ kpc, sufficient to resolve dense gas clumps in the ICM. The dark matter particle mass in the region surrounding the cluster is $9 \times 10^8 h^{-1} M_\odot$, while the rest of the simulation volume is followed with lower mass and spatial resolution. We refer readers to N07 for further details. CL101 is a massive, dynamically active cluster, which has recently experienced violent mergers (at $z \sim 0.1$ and $z \sim 0.25$) and contains two major substructures near the core at $z = 0$. These two substructures have been identified by visual inspection and masked out before its analysis. CL104 is a similarly massive but dynamically relaxed cluster, with no significant mergers occurred in the last 8 Gyrs.

In our previous work (Nagai et al. 2013), we investigated effects of baryonic physics on the velocity structure of the ICM, by analyzing CL104 and CL101 performed with varying gas physics. The first set is performed with non-radiative gas physics. The second set includes radiative cooling, star formation, metal enrichment, and stellar feedback (CSF). The third set includes CSF and energy feedback from AGN (CSF+AGN). By comparing these three runs, we found that, while the baryonic physics can have significant impact on the properties of cluster cores, the velocity structure outside the cluster core ($r \gtrsim 0.15r_{500}$) is relatively unaffected by the baryonic physics. Since the present work concerns measurements of large-scale gas motions outside of cluster cores regions, we focus our analyses on the non-radiative simulations and discuss their limitations and caveats in Section 4.

2.2. Mock ASTRO-H Simulations

We generate a mock ASTRO-H surface brightness map and spectrum for three orthogonal projection axes of each simulated cluster. The ASTRO-H pipeline consists of two main steps: (1) generation of the flux map from the simulation output; and (2) conversion of the flux map to a photon map by

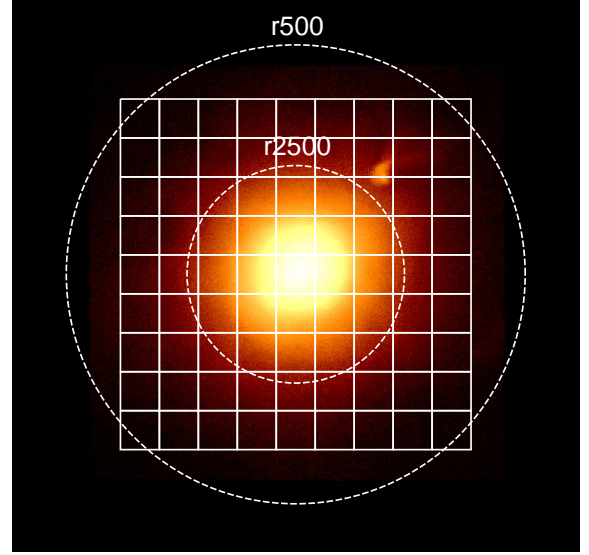


FIG. 1.— Mock ASTRO-H image of CL104 in the $[0.3, 10.0]$ keV band. 9×9 boxes, each with a size of $3' \times 3'$, were used for the analysis of projected velocity field. The grid (i, j) at the bottom-left corner is $(1, 1)$, and the grid label i/j indicates the cell located at the upward/rightward direction from the origin, respectively.

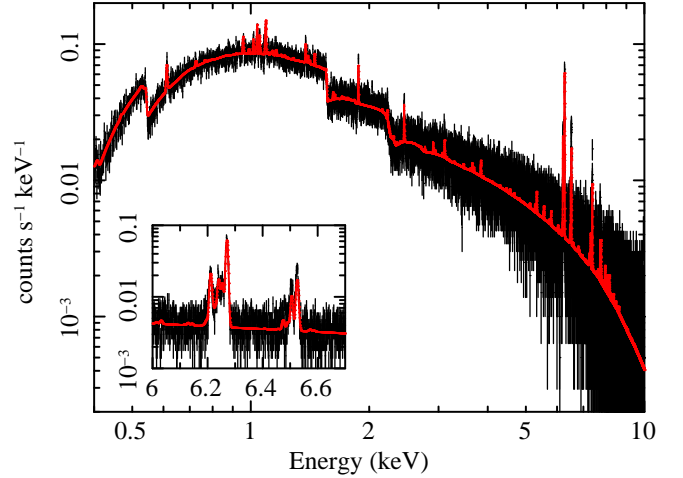


FIG. 2.— Mock ASTRO-H spectrum for the energy range $[0.3, 10.0]$ keV extracted from the grid $(i, j) = (7, 5)$ defined in Figure 1 of CL104 with total exposure time of 2 Ms. The inset shows the spectrum around the Fe XXV $K\alpha$ line (redshifted to 6.27 keV) where the velocity constraints come from. The redline shows the best model BAPEC fit of the spectrum.

convolving with the instrumental response of ASTRO-H. For the first step, we compute the emissivity ϵ_E as a function of energy E for each hydrodynamic cell using the APEC plasma code (Smith et al. 2001) with AtomDB version 2.0.2 (Foster et al. 2012). The emissivity $\epsilon_E = \epsilon_E(\rho, T, Z, z_{\text{obs}}, v_{\text{los}})$ is a function of the gas density ρ , temperature T , the gas metallicity $Z = 0.3Z_\odot$, and line-of-sight velocity v_{los} of the cell. The observed redshift of the clusters is set to $z_{\text{obs}} = 0.068$, which corresponds to the redshift of A1795, a nearby relaxed cluster, which is one of the likely targets for mapping out the gas velocity structure out to large radii with ASTRO-H. The energy range is $E \in [0.1, 10.0]$ keV with energy bin size of $\Delta E = 1$ eV, and we include the effect of thermal broadening on the emission lines.

Each flux map is computed by summing up the emis-

sivity of all cells contained within a sphere of radius of $5h^{-1}$ Mpc centered on the densest dark matter particle. We then convolve our flux map with the ASTRO-H ARF (`sxt-s_140505_ts02um_intall.arf`) and RMF (`ah_sxs_5ev_20130806.rmf`) response files from SIMX¹. The energy resolution of the RMF file is 5 eV. We then draw photons for each location from the convolved flux map assuming a Poisson distribution. As we are interested in the intrinsic systematics, such as projection effects, rather than statistical uncertainties, we set the exposure time $t_{\text{exp}} = 2$ Ms per pointing to ensure enough photons in the spectra. We do not model background noise because it is subdominant to the strong Fe XXV $K\alpha$ line where the gas velocity constraints come from.

2.3. ASTRO-H Data Analyses

In order to assess how accurately ASTRO-H can measure temperature and velocity structure in the ICM, we analyze the mock spectra and study how the physical parameters depend on various analysis conditions, fitting method, energy band, region selection, and deprojection. Unbinned spectra (1 spectral bin = 1 eV) are analyzed using the Cash statistic, while the data are rebinned so that each spectral bin contains at least 25 counts in the χ^2 fitting. Considering the size of the SXS field of view, the spectral regions are defined by $3' \times 3'$ grids (Figure 1) or annular rings with $3'$ width. The spectral fitting is performed by using XSPEC version 12.8. The spectral model consists of the BAPEC model and the Galactic absorption model (the `wabs` model; Morrison & McCammon 1983) and is convolved by the detector and telescope responses. The gas temperature, metal abundance, redshift, velocity dispersion, and the normalization are allowed to vary while the hydrogen column density is fixed at $N_H = 2 \times 10^{20} \text{ cm}^{-2}$, the value adopted when generating the mock simulations.² For metal abundance, the tables in Anders & Grevesse (1989) is used. The velocity dispersion is defined by the Gaussian sigma for velocity broadening. The bulk velocity along the line of sight is calculated by $c(z - z_{\text{cluster}})$ where z is the fitted redshift and $z_{\text{cluster}} = 0.068$. Figure 2 shows a mock ASTRO-H spectrum extracted from the grid $(i, j) = (7, 5)$ in Figure 1 of CL104 with total exposure time of 2 Msec.

The deprojection of annular spectra to recover the three-dimensional source properties is performed by the `project` model in XSPEC, assuming that the source emissivity is constant within the spherical shells whose radii correspond to the annuli used to extract the spectra. The quoted errors indicate 1σ errors.

To quantify the accuracies of velocity measurements from the mock data, we compare them against the “true” values measured directly from the simulations. Specifically, we compute the mass-weighted spherically averaged temperature and velocity profiles for each analyzed cluster following the procedure described in Lau et al. (2009). Briefly, we first define the rest frame of the cluster to be the mass-weighted dark matter velocity within r_{500} . We then compute the gas mass-weighted mean $\langle v \rangle_{\text{mw}}$ and root-mean-square velocity $\sqrt{\langle v^2 \rangle_{\text{mw}}}$ in this rest-frame. We define the “turbulent” velocity to be the velocity dispersion $\sigma_{\text{mw}} \equiv \sqrt{\langle v^2 \rangle_{\text{mw}} - \langle v \rangle_{\text{mw}}^2}$. We

¹ <http://hea-www.harvard.edu/simx/>

² The actual value of N_H toward A1795 is $1.2 \times 10^{20} \text{ cm}^{-2}$ according to the LAB survey of Galactic HI. This difference in N_H has no consequence on our results and conclusions of the paper.

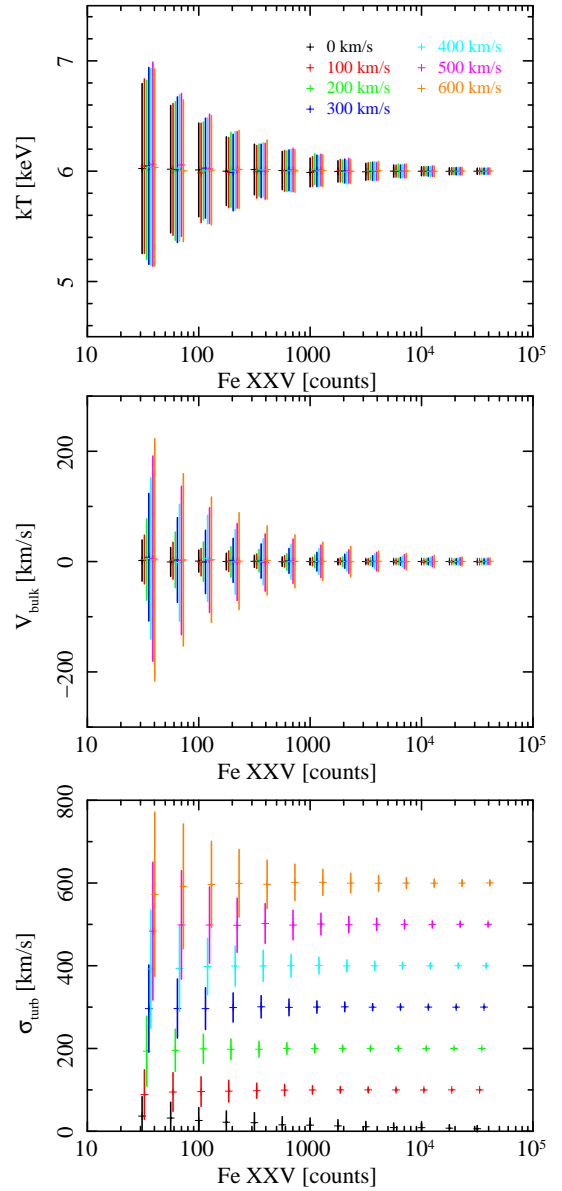


FIG. 3.— Temperature (top panel), bulk velocity (middle panel), and turbulent velocity (bottom panel) as a function of counts in the Fe XXV $K\alpha$ line complex from fitting faked spectra of the isothermal gas with $kT = 6.0$ keV, $Z = 0.3Z_{\odot}$ in 5.0–10 keV with the BAPEC model. Different colors indicate different input turbulent velocity $\sigma_{\text{turb}} = 0$ (black), 100 (red), 200 (green), 300 (blue), 400 (cyan), 500 (magenta), and 600 km s^{-1} (orange).

compute the “bulk” velocity as the projected mass-weighted velocity averaged along the line-of-sight.

3. RESULTS

3.1. Dependence on Photon Counts in the Fe XXV $K\alpha$ Line

The primary constraints on the ICM velocity measurements with ASTRO-H come from the shifting and broadening of the bright 6.7 keV Fe XXV $K\alpha$ line, therefore we first study the effect of photon counts in the Fe line on the parameter estimation. We simulated SXS spectra of isothermal gas assuming the BAPEC model with $kT = 6.0$ keV, $Z = 0.3Z_{\odot}$, and input turbulent velocity of $\sigma_{\text{turb}} = 0, 100, \dots, 600 \text{ km s}^{-1}$ and zero bulk velocity. To study the effects of photon counts, we vary the normalization so that the Fe XXV $K\alpha$ line complex contains 30 – 30000 counts. The simulated spectra in 5–10 keV

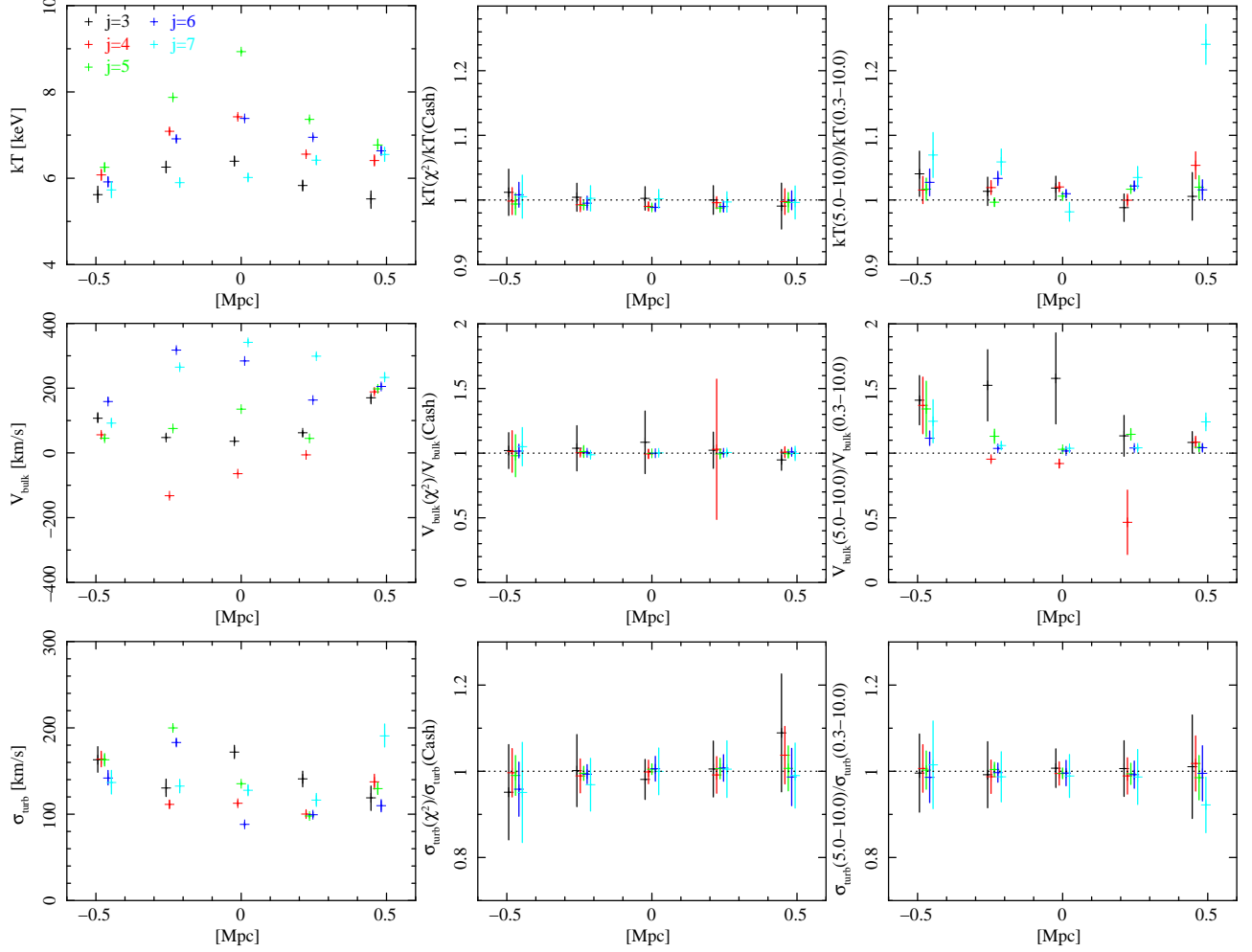


FIG. 4.— Left panels: results of the BAPEC model fitting to the 5.0–10.0 keV spectra using the Cash statistic for CL104. Middle panels: ratios of BAPEC model parameters from spectral fitting using the Cash and χ^2 statistic in the 5.0–10 keV band for CL104. Right panels: ratio of BAPEC model parameters from spectral fitting between 5.0–10 keV and 0.3–10 keV. The temperature (top panels), the bulk velocity (middle panels), and the turbulent velocity (bottom panels) are plotted along the i -axis of the map shown in Figure 1.

were fitted by the BAPEC model. Figure 3 shows the best-fit parameters and their 1σ statistical errors using Cash statistic. It shows that $\gtrsim 200$ counts in the Fe XXV $K\alpha$ line complex are required to measure the turbulent velocity accurately through line broadening for the assumed range of velocities. The error range in Figure 3 was derived by first simulating a large number of spectra and fitted the input model to each and compiled a histogram of the best-fit values from each trial and estimate the mean and the root-mean-square value. To achieve the accuracy better than 20%, > 200 counts are needed in the 6.7 keV Fe XXV $K\alpha$ line complex when the turbulent velocity $\sigma_{\text{turb}} < 200 \text{ km s}^{-1}$. We recommend > 200 counts in 6.7 keV Fe XXV $K\alpha$ line complex for robust measurements of σ_{turb} . Note that the requirement for calibration accuracy of SXS energy-scale is 2 eV with a goal of 1 eV (Mitsuda et al. 2014), which corresponds to the line shift of 90 km s^{-1} (or 45 km s^{-1}) at 6.7 keV. Thus, in very bright regions like cluster cores, the measurement is limited by the instrumental uncertainty rather than the statistical error.

3.2. Fitting Statistics: Cash vs. χ^2

Two statistics, Cash (Cash 1979) and χ^2 , are commonly used in X-ray spectral fitting. We compare how these two

statistics differ in the parameter estimation for the relaxed cluster CL104. Because velocity measurement requires sufficient photon counts (> 200 counts) in the Fe XXV $K\alpha$ line, the spectral regions are limited to the central 5×5 grids (approximately $r < r_{2500}$). The left panels of Figure 4 shows results of the BAPEC model fitting to the 5.0–10.0 keV spectra using the Cash statistic and the middle panels shows comparison of resultant parameters between Cash and χ^2 statistics. Each spectrum contains at least 200 counts in the Fe XXV $K\alpha$ line. The differences in the fitted temperature, bulk and turbulent velocities between the two different methods are typically less than 20%, which is reasonable as the Cash statistic approaches the χ^2 statistic in the limit of large photon counts. Since two methods produce consistent results, the unbinned spectra are analyzed by utilizing the Cash statistic in the following analysis. Cash statistic is preferred for low photon counts, the spectrum does not need to be rebinned as in the case of χ^2 statistic, thus preserving the spectral energy resolution crucial for measuring gas velocities from line broadening.

3.3. Spectral Energy bands and Multiphase ICM

The temperature of the ICM may affect the accuracies of turbulent velocity measurements from line broadening.

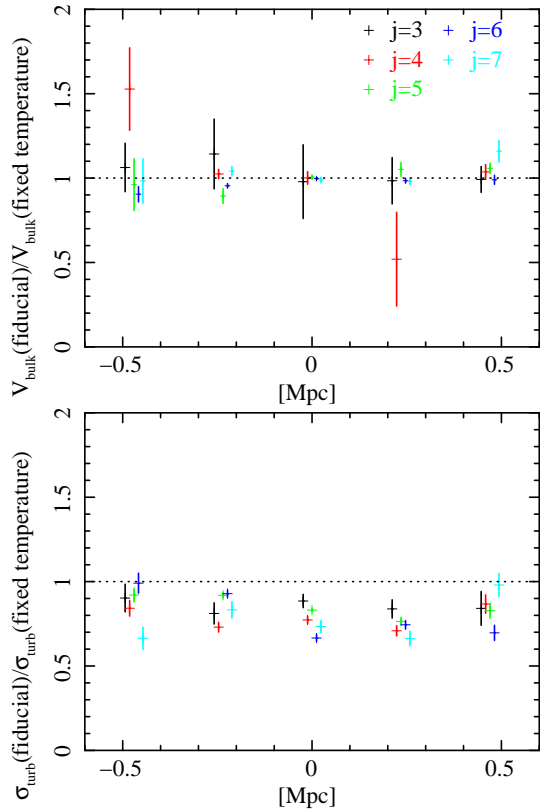


FIG. 5.— Comparison of bulk (top) and turbulent (bottom) velocities derived in the fiducial case with the true gas temperature and the fixed temperature case with $T_X = 7.7$ keV, for CL104. Different color points correspond to different j location in the map shown in Figure 1.

The line broadening originates from both thermal and turbulent motions and given by a combination of $\Delta E_{\text{th}} = E_0(kT/m)^{1/2}c^{-1}$ and $\Delta E_{\text{turb}} = E_0\sigma_{\text{turb}}c^{-1}$, where E_0 is the rest-frame energy of the line emission, and m is the ion mass. Since the temperature kT is determined primarily by the shape of continuum spectrum of the hot ICM, it is ideal to use a wider energy range for accurate parameter estimation. If a certain amount of cool gas exists along the line of sight, the soft emission may affect the temperature determination even though the emissivity of Fe XXV $K\alpha$ line at low temperature is low. We thus compare analysis in two different energy ranges, 5.0–10 keV and 0.3–10 keV, where the latter includes more emission from cool gas.

As seen from the right panels in Figure 4, for the relaxed cluster CL104, the fitted parameters do not depend on the choice of the energy range for most regions except for the grid $(i, j) = (7, 7)$, where the temperature derived from 5.0–10 keV is $\sim 25\%$ higher than that derived from 0.3–10 keV. This is due to the presence of an infalling cooler substructure which is visible in the north-west of the cluster image, shown in Figure 1.

The recovered turbulent velocity does not show clear dependence on the energy range. This is expected as most of the constraints on the turbulent velocity come from the broadening of the Fe XXV $K\alpha$ line present in both energy ranges. Since the velocity constraints from line broadening is inversely proportional to the mass of the ion species, velocity measurements based on the Doppler broadening of the Fe XXV $K\alpha$ ion is least affected by thermal broadening compared to emission lines of species of lighter elements (e.g.,

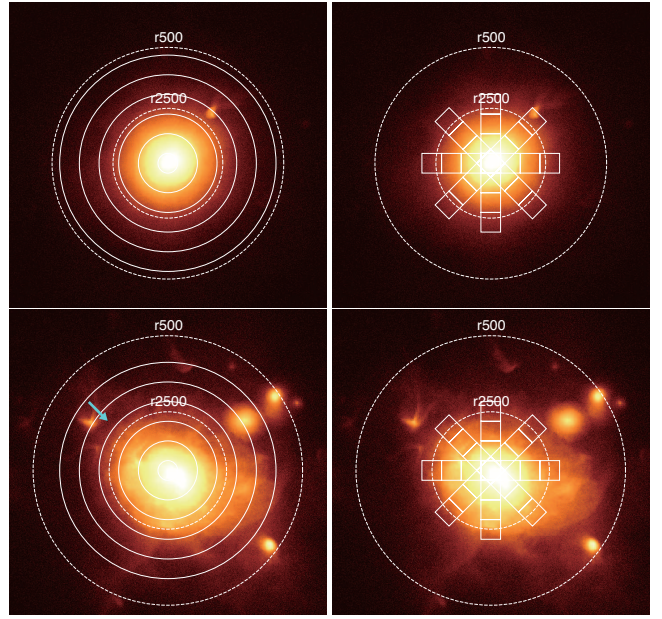


FIG. 6.— Top panels: spectral regions for the deprojection analysis for CL104: 6 annuli (left) and 4 boxes in 8 azimuthal directions (right). Bottom panels: the same regions are shown for CL101. The maps show the x-projections for the two clusters. The location of merger shock is indicated by the arrow (see §3.4.3).

Inogamov & Sunyaev 2003). On the other hand, the soft band (0.3–5.0 keV) contains emission lines from lighter elements which are more susceptible to thermal broadening, and leads to biases in turbulent velocity estimates.

We further examine the effects of multiphase ICM by fixing the gas temperature to 7.7 keV, while keeping the gas density, abundance, exposure time and fitting method unchanged. The velocities in this case should be unbiased from the effects of the multi-temperature ICM. We compare the velocity estimates between the fixed temperature case and the fiducial, multi-temperature case in Figure 5. While the bulk velocity measurements of the two cases are consistent with each other within statistical errorbars, the turbulent velocity is underestimated by $\sim 30\%$ in the fiducial case compared to the fixed temperature case. This is expected because the turbulent velocity (determined from broadening of the Fe XXV $K\alpha$ line) is more affected by higher temperature gas through thermal broadening, while the bulk velocity (determined from line shift) is not.

3.4. Velocity Profiles

3.4.1. Deprojection analysis

One of the key science goals of ASTRO-H is to measure non-thermal pressure profile due to bulk and turbulent gas motions and their impact on the hydrostatic mass. The non-thermal pressure profile is determined from spherically averaged density and velocity profiles. To study how well we can recover three-dimensional temperature and velocity profiles from the ASTRO-H spectra, we extract 0.3–10 keV spectra from annular rings with $3'$ width (top left panel in Figure 6) and fitted them with the BAPEC model.

Figure 7 show the projected and deprojected quantities for the x , y , z projections for a relaxed cluster CL104. Since CL104 is a relatively relaxed, spherically symmetric cluster, the temperature and turbulent and bulk velocities from the three orthogonal projections agree with each other to within

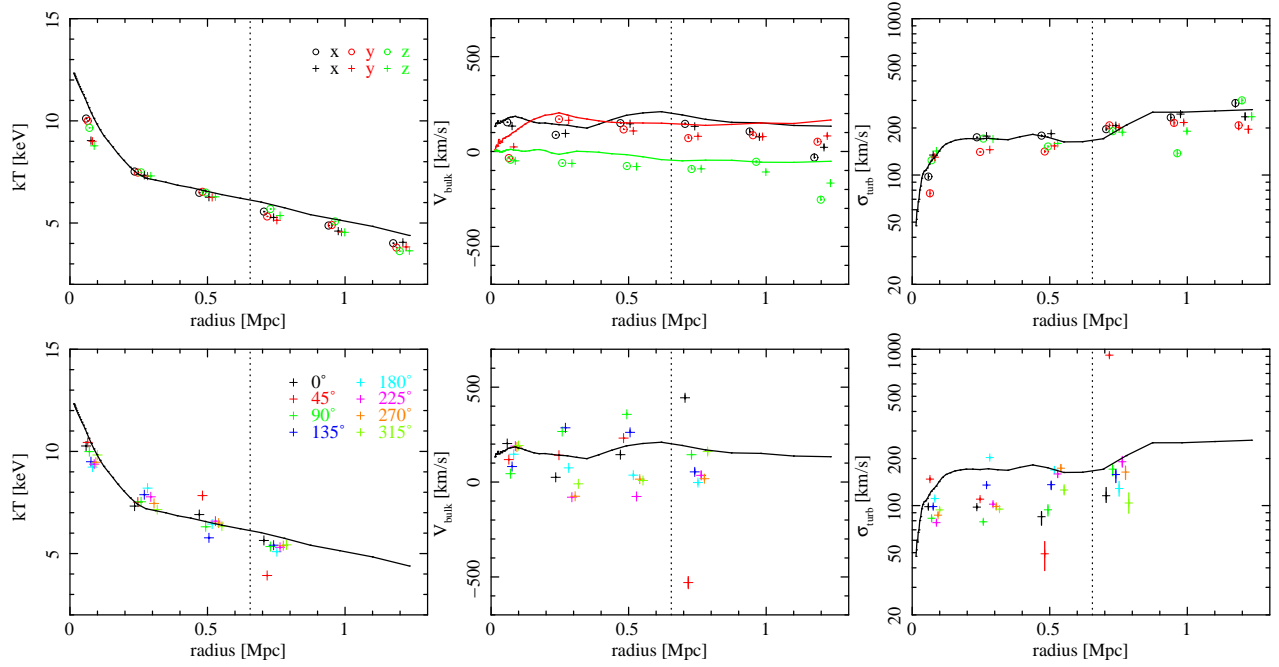


FIG. 7.— Top panels: Deprojected temperature (left panels), bulk velocity (middle panels), and turbulent velocity (right panels) of the relaxed cluster CL104 viewed along three orthogonal projections: x (black), y (red), z (green) projections (open circles). The projected quantities are shown with the crosses for comparison. Bottom panels: Deprojected temperature, bulk velocity, and turbulent velocity for the 8 azimuthal directions (crosses) for the x projection. The Cash statistic was used to fit the 0.3–10 keV spectra. The solid lines indicate mass-weighted, spherically averaged values computed directly from the simulation, and the dotted line indicates r_{2500} of the cluster.

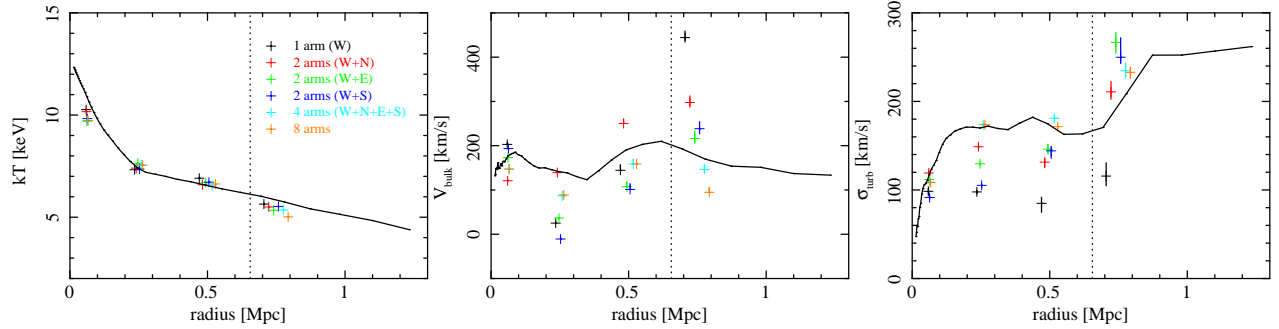


FIG. 8.— Effects of sample size. Results of deprojection analysis for spectra extracted from 1 arm (W), 2 arms (W+N, W+E, W+S), 4 arms (W+N+E+S), and 8 arms are plotted. Deprojected temperature (top panels), bulk velocity (middle panels), and turbulent velocity (bottom panels) of the relaxed cluster CL104 viewed along the x projection (crosses). The Cash statistic was used to fit the 0.3–10 keV spectra. The circles indicate deprojected values. The solid lines indicate mass-weighted, spherically averaged values computed directly from simulation, and the dotted line indicates r_{2500} of the cluster.

about 10%. Furthermore, we find that the deprojected values are in agreement with the mass-weighted, spherically averaged profiles measured directly from the simulation to within $\lesssim 20\%$. Note, however, that the recovered turbulent velocity tends to be underestimated by 10% in some annuli, particularly in the outer regions ($r \gtrsim r_{2500}$) where the photon counts in the Fe XXV K α line drops below 200.

3.4.2. Azimuthal Variations

Since the Field-Of-View (FOV) of SXS is small, we need to perform mosaic observations with multiple pointings to cover the spatially extended regions at large cluster-centric radii. However, since accurate velocity measurements require fairly deep exposures ($\gtrsim 100$ ks at $r \approx r_{2500}$), it would be costly to perform mosaic observations. In practice, observations at the large cluster-centric radii will be limited a few directions.

Since the cluster gas is not perfectly spherically symmetric and its velocity distribution is generally anisotropic, we expect that the velocity profile measured along any given direction is not representative of the azimuthally averaged velocity profile in an annular ring.

In order to investigate the level of the azimuthal variations in the recovered velocity profiles, we extract spectra from four grids at $r \lesssim r_{2500}$ in eight azimuthal directions: 0°, 45°, 90°, 135°, 180°, 225°, 270°, and 315° from the horizontal, corresponding to W, NW, N, NE, E, SE, S, and SW (top right panel in Figure 6). The deprojected temperature and velocity profiles of the 8 azimuthal directions in the x projection is plotted in Figure 7 for CL104 in the left and right panels respectively.

Even in the relaxed cluster CL104, we find significant scatter in the fitted temperature, bulk and turbulent velocities among different azimuthal directions. The azimuthal varia-

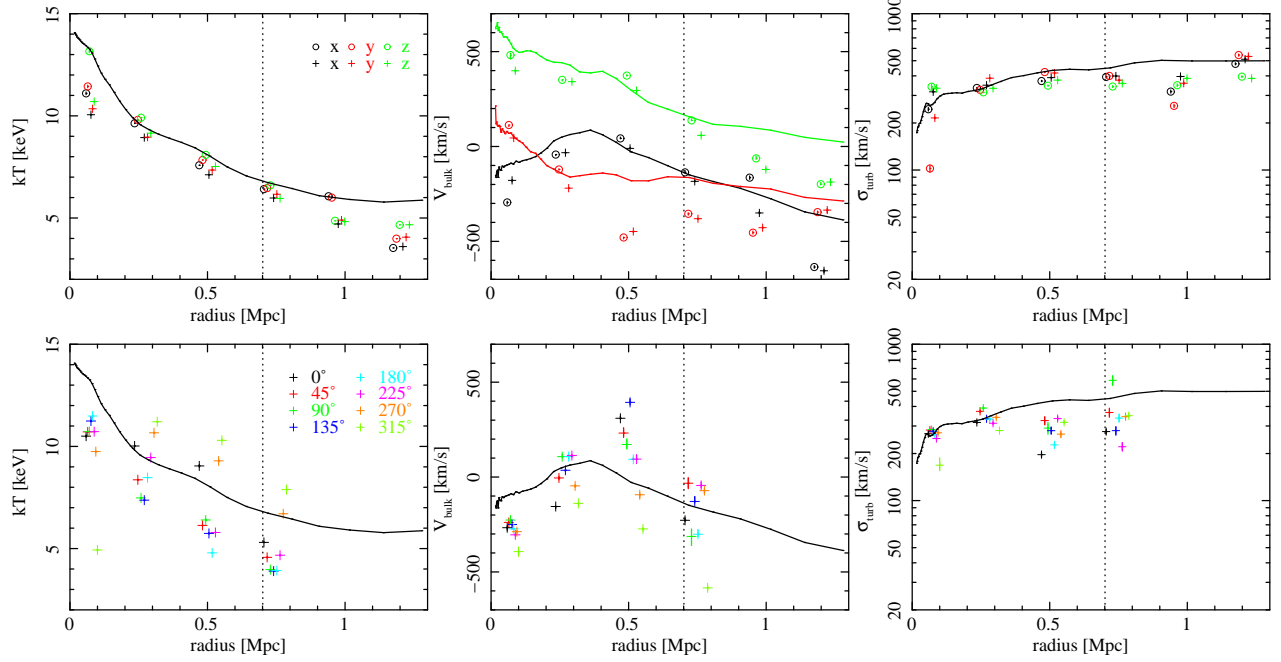


FIG. 9.— Same as Figure 7 for the merging cluster CL101.

tion in the projected temperature increases with radius from 10% at $r = 0.2r_{2500}$ to 30% at $r = r_{2500}$. The temperature variation in the outer bin is driven by the infalling cold substructure in the NW direction. The same substructure is also partly responsible for the large differences in the bulk and turbulent velocities.

These results suggest that the velocity profile measured along any single arm is not representative of the spherically averaged profile. Specifically, the deprojected turbulent velocities along any single direction systematically underestimate the spherically averaged turbulent velocity measured directly from the simulation (shown in the bottom-right panel of Figure 7), because the simple spherical analysis fails to capture the azimuthal variations in the bulk velocities (shown the bottom-middle panel of Figure 7). Such variations in the bulk velocities are expected, because mergers and filamentary accretions occur anisotropically along the axes of mergers and filaments, respectively.

In general, decomposition of gas motions into *turbulent* and *bulk* components, inferred from broadening and shifting of X-ray emission lines respectively, depends on the size and geometry of the regions where the X-ray spectra were extracted (see the Appendix for more discussion). To study the dependence of velocity recovery on the size of the regions, we co-added spectra at the same radii in different pointing directions (e.g., W and N) and performed the deprojection analysis. Figure 8 shows the resulting recovered temperature, bulk, and turbulent velocity when the spectra in 2, 4 or 8 arms are combined. Compared to the results of a single arm, the turbulent/bulk velocity converges to the spherically averaged values when we combine spectra from more arms. This suggests that sampling more multiple directions leads more robust estimates of the velocity profiles. Having 8 arms leads to better recovery of the velocity profiles to about 20%.

3.4.3. Dependence on Dynamical States

Next, we repeat the same deprojection and azimuthal analyses on the merging cluster CL101. The bottom left and right panels of Figure 6 show the regions selected for these analyses, respectively. Figure 9 shows its deprojected profiles for the temperature, bulk and turbulent velocities in annular bins and in the 8 azimuthal directions, compared with the simulation values. In general, the temperature and turbulent velocities from the annular analysis recover the true values quite well, although the scatter among different orthogonal projections are greater than that of CL104. The recovery of the bulk velocities is generally accurate to within 20% at $r \lesssim r_{2500c}$, but it is underestimated at larger radii where there is a merger shock (the approximate location is indicated in Fig. 6). The azimuthal variations in both temperature and velocities are also larger for the unrelaxed cluster CL101.

3.5. Hydrostatic Mass Bias

One of the primary sources of astrophysical uncertainties in cluster cosmology lies in hydrostatic mass bias due to non-thermal pressure support provided by internal gas motions in the ICM. Assuming spherical symmetry, the total cluster mass within some radius r can be expressed as the following:

$$M(< r) \cong M_{\text{HSE}} + M_{\text{rand}} + M_{\text{rot}} + M_{\text{accel}}. \quad (1)$$

where M_{HSE} is the hydrostatic mass, M_{rand} is the mass term associated with random (or turbulent) gas motions, M_{rot} is the term associated with the rotational gas motions, and M_{accel} is the term associated with acceleration (or deceleration) of gas (see Lau et al. 2013, for details). Note that other mass terms are negligible ($\lesssim 1\%$) compared to M_{rand} , M_{rot} (Lau et al. 2009) and M_{accel} (Nelson et al. 2014). The hydrostatic mass is given by

$$M_{\text{HSE}} = \frac{-rkT}{G\mu m_p} \left(\frac{\partial \log \rho}{\partial \log r} + \frac{\partial \log T}{\partial \log r} \right), \quad (2)$$

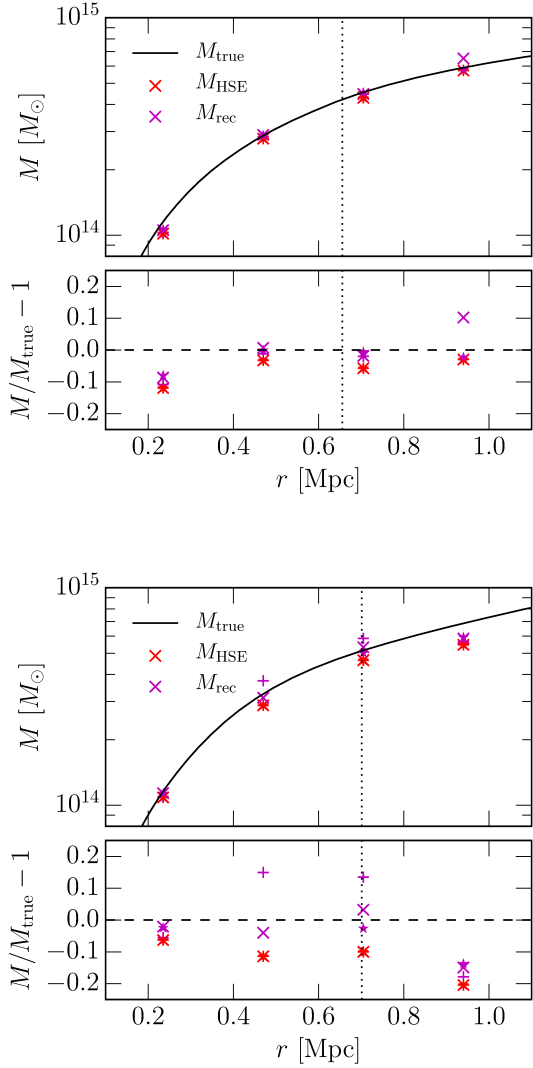


FIG. 10.— Recovery of the hydrostatic mass bias in the relaxed cluster CL104 (top panel) and the merging cluster CL101 (bottom panel). Upper panels: The black line represents the true mass profile measured directly from simulation, the red points represent the hydrostatic mass M_{HSE} measured from simulation, and the magenta points represent the recovered mass profile, $M_{\text{rec}} = M_{\text{HSE}} + M_{\text{rand}} + M_{\text{rot}}$, using the velocity measurements from ASTRO-H mocks. Lower panels: Profiles of the hydrostatic mass bias, $M_{\text{HSE}}/M_{\text{true}} - 1$ (red points) and the recovered mass, $M_{\text{rec}}/M_{\text{true}} - 1$ (magenta points). Different symbols indicate the recovered mass M_{rec} obtained from the ASTRO-H mock maps viewed along three orthogonal projections of each cluster. The vertical dotted lines indicate r_{2500c} for each cluster.

where T and ρ are the mass-weighted gas temperature and gas density, respectively. Note that the hydrostatic mass depends on the gradients of gas temperature and gas density, which may not be well determined with ASTRO-H owing to its relatively poor spatial resolution of $1'3$. The mass terms due to velocity M_{rand} and M_{rot} , however, are less sensitive to resolution because both the average bulk and turbulent velocities do not change significantly with cluster-centric radius, and thus

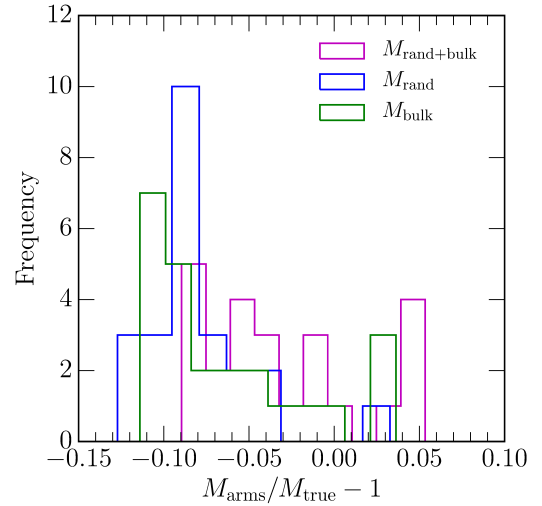
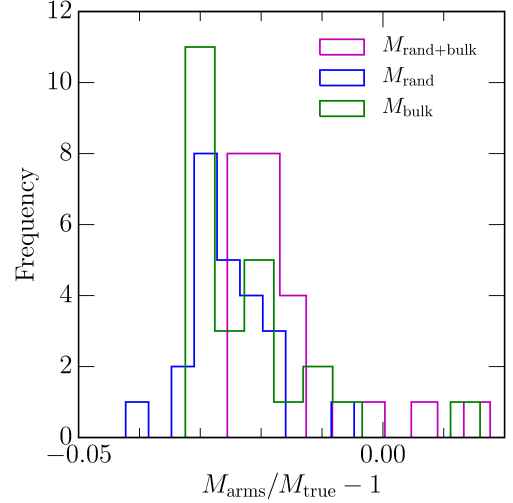


FIG. 11.— Histograms of the mass bias of the recovered mass, $M_{\text{rec}}/M_{\text{true}} - 1$, at $r = 0.5$ Mpc, computed from the deprojected bulk and turbulent velocity measurements along individual azimuthal arms for the relaxed cluster CL104 (top panel) and the merging cluster CL101 (bottom panel). The magenta lines represent the recovered mass computed from combined turbulent and bulk motion measurements, while the blue and green lines represent the mass computed using only random and bulk motions, respectively.

can be determined rather well with ASTRO-H:

$$M_{\text{rand}} = \frac{-r^2}{G\rho} \frac{\partial \rho \sigma_r^2}{\partial r} - \frac{r}{G} (2\sigma_r^2 - \sigma_t^2), \quad (3)$$

$$M_{\text{rot}} = \frac{r}{G} \langle v_{\text{rot}} \rangle^2, \quad (4)$$

where σ_r^2 and σ_t^2 are the mass-weighted velocity dispersion for the radial and tangential component, and $\langle v_{\text{rot}} \rangle$ is the mass-weighted mean rotational velocity. The computation of these mass terms requires three-dimensional velocity fields that are not directly accessible to ASTRO-H observations. Only observationally accessible quantities are line-of-sight measurements of turbulent velocity (σ_{LOS}) and bulk velocity (v_{LOS}) measured using broadening and shifting of X-ray emission lines, respectively. To estimate M_{rand} from observational data,

we assume the gas velocity dispersion is isotropic, meaning that the measured line-of-sight turbulent velocity is equal to the isotropic one-dimensional velocity dispersion: $\sigma_{\text{LOS}}^2 = \sigma_{\text{1D}}^2 = \sigma_r^2 = \sigma_t^2/2$. Note that hydrodynamical simulations suggest that, while gas velocity dispersion is isotropic around our radius of interest ($r_{2500} \leq r \leq r_{500}$) on average, it can be fairly anisotropic for individual clusters with $\beta = 1 - \sigma_t^2/(2\sigma_r^2) \approx \pm 0.5$ (e.g., see Figure 1 in Lau et al. 2009), leading to scatter in M_{rand} . For M_{rot} , we estimate the rotational velocity $\langle v_{\text{rot}} \rangle$ as the difference in the line-of-sight bulk velocity (v_{LOS}) between two opposite regions; e.g., $\langle v_{\text{rot}} \rangle \approx |v_{\text{LOS,NW}} - v_{\text{LOS,SE}}|$ where $v_{\text{LOS,NW}}$ and $v_{\text{LOS,SE}}$ are line-of-sight bulk velocities in the NW and SE directions. Note that this estimate of the rotational velocity assumes that the axis of rotation lies in the plane of the sky, which is not necessarily true.

The upper panels of Figure 10 show the mass profiles of the two clusters: CL104 (top panel) and CL101 (bottom panel). The black lines represent the true mass profile measured directly from simulation, the red lines represent the hydrostatic mass M_{HSE} measured from simulation, and the magenta points represent the recovered mass $M_{\text{rec}} = M_{\text{HSE}} + M_{\text{rand}} + M_{\text{rot}}$, with the latter two terms computed with velocity profile measurements from ASTRO-H mocks. Different symbols indicate the recovered mass M_{rec} obtained from the ASTRO-H mock maps viewed along three orthogonal projections of each cluster. The lower panels of Figure 10 show the profiles of the HSE mass bias and the recovered mass, relative to the true cluster mass, for the same clusters. The HSE mass bias is shown in red, and the bias of the recovered masses $M_{\text{rec}} = M_{\text{HSE}} + M_{\text{rand}} + M_{\text{rot}}$ is shown in magenta.

In the lower panels, we demonstrate that ASTRO-H cluster observations can be used to recover the total cluster mass at $r \gtrsim r_{2500}$ at the level of about 5% for dynamically relaxed clusters, provided that we measure and correct for both M_{rand} (random motion) and M_{rot} (rotational motion) terms (see the appendix for more discussion). For example, for the relaxed cluster CL104, the remaining bias in the corrected mass, $M_{\text{rec}}/M_{\text{true}} - 1$, varies from +1% to -4% in the outer three bins, compared to -3% to 7% for the HSE mass. For the unrelaxed cluster CL101, the improvement in mass measurements is more evident; i.e., the remaining bias in the corrected mass, $M_{\text{rec}}/M_{\text{true}} - 1$, improves from -9% to +3% in the inner bins. However, the mass recovery is not as good in the outer bins, because the gas is not in steady-state.

As shown in Section 3.4.2, the velocity measurements along individual azimuthal arms are not representative of spherically averaged velocity profiles, which could introduce biases in the recovered mass. Here, we demonstrate that this mass bias due to azimuthal variations in velocity can be mitigated provided that we account for both bulk and random and turbulent gas motions from line shifts and broadening, respectively. In Figure 11, we show the histograms of the recovered mass computed from the deprojected bulk and turbulent velocities in each azimuthal arm, compared to true cluster mass at $r = 0.5$ Mpc. Note that we have made the assumption that the rotational velocity is equal to the deprojected bulk velocity. For the relaxed cluster CL104, the recovered mass for a single arm computed from only turbulent (bulk) motions underestimates the true mass by -4 (-1)%. The mass recovery improves when we include both random and bulk motions, leading to smaller biases: -3% to +2%. For the merging cluster CL101, the mass recovery from a single arm also improves if we consider both bulk and turbulent motions.

4. DISCUSSION

There are several effects that are missing from the present mock ASTRO-H analysis. We briefly discuss their effects on our results.

Point Spread Function: A systematic effect may arise from scattering of photons by a relatively wide Point Spread Function (PSF) of the SXT onboard ASTRO-H. The half power diameter is $1.3'$ (Takahashi et al. 2014). Strongly peaked X-ray emission at the center of relaxed cluster may contaminate the measurement of turbulent velocity at fainter, outer regions. Abundance peak in cool core clusters will result in stronger contamination. In the case of A1795, the fraction of scattered photons in a SXS field of view placed at the scale radius r_{2500} from adjacent regions is estimated to be 25% based on SXS simulations assuming the azimuthally-averaged PSF model. This effect can be corrected by simultaneously analyzing a series of pointings along the radius from the center and solving intrinsic distributions of the line shifts and width (see, ASTRO-H White Paper on Clusters of Galaxies and Related Science by Kitayama et al. 2014).

Baryonic physics: The results presented in this paper are based on non-radiative simulations that do not include baryonic effects such as radiative cooling, star formation, and AGN feedback. These baryonic physics can alter the velocity structure of the ICM especially in cluster cores, where their effects are significant (Nagai et al. 2013). Radiative cooling and star formation produces the multiphase ICM structure through thermal instability (e.g., Voit & Donahue 2015), but the cooling flow is regulated by periodic bursts of outflows from the central AGN (e.g., Fabian 2012; Zhuravleva et al. 2014), generating the complex ICM structure in this region. However, the velocity structure outside the cluster core ($r \gtrsim 0.15r_{500}$) is relatively unaffected by the baryonic physics (Nagai et al. 2013). Furthermore, the ICM temperature has shown to be more homogeneous outside the cluster core with the inclusion of baryon dissipation (Rasia et al. 2014), suggesting that the systematic uncertainties due to temperature inhomogeneities should be smaller.

Resonant Scattering: We did not include the effects of resonant scattering, e.g., in the Fe XXV line (Zhuravleva et al. 2011; Shang & Oh 2013). Resonant scattering increases the optical depth and suppresses the strength of the emission line. The effect of resonant scattering can be important in most central region of the cluster where the density, and therefore the optical depth to the 6.7 keV Fe XXV $K\alpha$ line is high. Outside the central region, however the effect is expected to be small. In the presence of turbulent motions, resonant scattering is suppressed by Doppler shifting the line out of resonance. Adding the effect of resonant scattering should therefore improve the velocity recovery of ASTRO-H as it provides additional constraints from the shape of the resonant line (e.g., Zhuravleva et al. 2013).

5. CONCLUSIONS

Gas motions play an important role in determining the properties of the hot X-ray emitting ICM and constraining cosmological parameters using X-ray and SZ effect observations of galaxy clusters. Despite their importance, we know very little about the nature of gas motions in the ICM. The upcoming ASTRO-H mission will provide the first direct measurements of gas motions in galaxy clusters through Doppler shifting and broadening of X-ray emission lines. In this work, we investi-

gate how well ASTRO-H can measure the bulk and turbulent gas motions in the ICM by analyzing mock ASTRO-H maps and spectra of simulated clusters extracted from hydrodynamical cosmological simulations. We summarize our main findings below:

1. ASTRO-H measurements of the bulk and random velocities are accurate to $\lesssim 20\%$, when the number of photons exceeds 200 in the 6.7 keV Fe XXV $K\alpha$ line complex. This enables ASTRO-H to make velocity velocity measurements out to $r \lesssim r_{2500}$ along any given arm of a nearby rich galaxy clusters with a reasonable exposure time ($\lesssim 100$ ks). However, ASTRO-H velocity measurements become increasingly more expensive, requiring deep exposure ($\gtrsim 1$ Ms) in the low surface brightness region in the outskirts of galaxy clusters.
2. Velocity measurements using only the hard (5.0 – 10 keV) band of the X-ray spectrum achieve similar accuracies as those based on the full (0.3 – 10 keV) band as both bands contain the 6.7 keV Fe XXV $K\alpha$ line. However, using the soft (0.3 – 5.0 keV) band spectrum alone introduces a significant bias, as the emission lines in this band come from low mass ions that are more susceptible to thermal broadening, making the effect of Doppler broadening more difficult to discern.
3. Spectra extracted from annular bins give a good recovery of the thermodynamic and velocity profiles of the ICM. Specifically, deprojected temperature and velocity profiles from spectra extracted from the annular bins agree well with the “true” mass-weighted, spherically averaged profiles computed directly from the simulations to better than 20%.
4. We find significant azimuthal variations in the recovered turbulent velocities, by up to a factor of 2, even in dynamically relaxed clusters. Our finding suggests that the velocity structure of the ICM is richer and more complex than its thermodynamic counterpart. Measurement of the turbulent velocity profile in any given azimuthal direction (or arm) is, therefore, not representative of the underlying mass-weighted, spherically averaged profile, which is required to correct for the hydro-

static mass bias. Since the field of view of ASTRO-H SXS is small, mosaic observations are required to sample the annular regions at the large cluster-centric radii of nearby clusters, which could be expensive and infeasible. Our results suggest that combining spectra from eight arms leads to better recovery of the velocity profiles to about 20%.

5. We demonstrate that ASTRO-H observations can be used to recover the total cluster mass at $r \lesssim r_{2500}$ at the level of 5% for dynamically relaxed clusters, provided that we measure and correct for mass biases associated with both random and rotational motions. The remaining uncertainties arise from the assumptions on the isotropy of random gas motions and projection effects on recovered bulk velocities. Note that accurate measurements of the hydrostatic mass require high-angular resolution X-ray instruments, such as *Chandra* and *XMM-Newton*, and ASTRO-H (with limited angular resolution) provides the hydrostatic mass bias associated with bulk and random gas motions.

Although our analyses have focused on ASTRO-H, some of these results are broadly applicable to future X-ray missions, such as *Athena+*³ and *SMART-X*⁴. Future missions will improve sensitivities and angular resolutions, produce spatially-resolved velocity structure in the ICM, and enable measurements of the ICM velocity power spectrum (Zhuravleva et al. 2012). However, future measurements will be increasingly limited by systematic uncertainties (associated e.g., with multiphase ICM and dynamical state of clusters) rather than statistical uncertainties. Future work must address how to separate bulk and turbulent motions, how well do different codes agree on the gas velocity field, and what are the main drivers of bulk and turbulence motions.

We acknowledge Miyu Masuyama for her contribution to the early stage of this work and Eugene Churazov, Kyoko Matsushita, Takaya Ohashi, Andrew Szymkowiak and Irina Zhuravleva for discussions and/or comments on the manuscript. This was supported in part by JSPS, KAKENHI grant 25400231, NSF grant AST-1412768 & AST-1009811, NASA ATP grant NNX11AE07G, NASA Chandra Theory grant GO213004B, the Research Corporation, and by the facilities and staff of the Yale Center for Research Computing.

REFERENCES

- Allen, S. W., Rapetti, D. A., Schmidt, R. W., et al. 2008, *MNRAS*, 383, 879
 Anders, E., & Grevesse, N. 1989, *Geochim. Cosmochim. Acta*, 53, 197
 Battaglia, N., Bond, J. R., Pfrommer, C., & Sievers, J. L. 2012, *ApJ*, 758, 74
 Cash, W. 1979, *ApJ*, 228, 939
 Churazov, E., Vikhlinin, A., Zhuravleva, I., et al. 2012, *MNRAS*, 421, 1123
 Etori, S., Donnarumma, A., Pointecouteau, E., et al. 2013, *Space Sci. Rev.*, 177, 119
 Fabian, A. C. 2012, *ARA&A*, 50, 455
 Foster, A. R., Ji, L., Smith, R. K., & Brickhouse, N. S. 2012, *ApJ*, 756, 128
 Inogamov, N. A., & Sunyaev, R. A. 2003, *Astronomy Letters*, 29, 791
 Kitayama, T., Bautz, M., Markevitch, M., et al. 2014, *ArXiv e-prints*, arXiv:1412.1176
 Klypin, A., Kravtsov, A. V., Bullock, J. S., & Primack, J. R. 2001, *ApJ*, 554, 903
 Kravtsov, A. V. 1999, PhD thesis, New Mexico State Univ.
 Kravtsov, A. V., Klypin, A., & Hoffman, Y. 2002, *ApJ*, 571, 563
 Lau, E. T., Kravtsov, A. V., & Nagai, D. 2009, *ApJ*, 705, 1129
 Lau, E. T., Nagai, D., & Nelson, K. 2013, *ApJ*, 777, 151
 Miniati, F. 2015, *ApJ*, 800, 60
 Mitsuda, K., Kelley, R. L., Akamatsu, H., et al. 2014, *Proc. SPIE*, 9144, 2
 Morrison, R., & McCammon, D. 1983, *ApJ*, 270, 119
 Nagai, D., Kravtsov, A. V., & Vikhlinin, A. 2007a, *ApJ*, 668, 1
 Nagai, D., Lau, E. T., Avestruz, C., Nelson, K., & Rudd, D. H. 2013, *ApJ*, 777, 137
 Nagai, D., Vikhlinin, A., & Kravtsov, A. V. 2007b, *ApJ*, 655, 98
 Nelson, K., Lau, E. T., Nagai, D., Rudd, D. H., & Yu, L. 2014, *ApJ*, 782, 107
 Nelson, K., Rudd, D. H., Shaw, L., & Nagai, D. 2012, *ApJ*, 751, 121
 Ota, N., Fukazawa, Y., Fabian, A. C., et al. 2007, *PASJ*, 59, 351
 Planck Collaboration. 2015, *A&A*, submitted, arXiv:1502.01597
 Rasia, E., Etori, S., Moscardini, L., et al. 2006, *MNRAS*, 369, 2013
 Rasia, E., Lau, E. T., Borgani, S., et al. 2014, *ApJ*, 791, 96
 Rudd, D. H., Zentner, A. R., & Kravtsov, A. V. 2008, *ApJ*, 672, 19
 Sanders, J. S., & Fabian, A. C. 2013, *MNRAS*, 429, 2727
 Schuecker, P., Finoguenov, A., Miniati, F., Böhringer, H., & Briel, U. G. 2004, *A&A*, 426, 387
 Shang, C., & Oh, S. P. 2013, *MNRAS*, 433, 1172
 Shi, X., & Komatsu, E. 2014, *MNRAS*, 442, 521

³ <http://athena2.irap.omp.eu/>

⁴ <http://smart-x.cfa.harvard.edu/>

Shi, X., Komatsu, E., Nelson, K., & Nagai, D. 2015, *MNRAS*, 448, 1020
 Smith, R. K., Brickhouse, N. S., Liedahl, D. A., & Raymond, J. C. 2001, *ApJ*, 556, L91
 Takahashi, T., Mitsuda, K., Kelley, R., et al. 2014, *Proc. SPIE*, 9144, 25
 Tamura, T., Hayashida, K., Ueda, S., & Nagai, M. 2011, *PASJ*, 63, 1009
 Vazza, F., Brunetti, G., Gheller, C., Brunino, R., & Brüggén, M. 2011, *A&A*, 529, A17
 Vazza, F., Brunetti, G., Kritsuk, A., et al. 2009, *A&A*, 504, 33
 Vikhlinin, A., Kravtsov, A. V., Burenin, R. A., et al. 2009, *ApJ*, 692, 1060
 Voit, G. M., & Donahue, M. 2015, *ApJ*, 799, L1
 Zhuravleva, I., Churazov, E., Kravtsov, A., et al. 2013, *MNRAS*, 428, 3274

Zhuravleva, I., Churazov, E., Kravtsov, A., & Sunyaev, R. 2012, *MNRAS*, 422, 2712
 Zhuravleva, I., Churazov, E., Schekochihin, A. A., et al. 2014, *Nature*, 515, 85
 Zhuravleva, I. V., Churazov, E. M., Sazonov, S. Y., Sunyaev, R. A., & Dolag, K. 2011, *Astronomy Letters*, 37, 141
 ZuHone, J., Markevitch, M., & Zhuravleva, I. 2015, *ApJ*, submitted, arXiv:1505.07848

APPENDIX

DECOMPOSITION OF BULK AND RANDOM GAS MOTIONS AND HYDROSTATIC MASS BIAS

In Lau et al. (2013), we showed that there are two methods for measuring hydrostatic mass bias from gas motions, and that they are mathematically equivalent. Here we give a brief review of the two methods. The first method, called the “Summation method”, is based on Gauss’s Law and Euler’s Equation, where the cluster mass within some volume V with surface ∂V . Assuming steady-state of gas (for simplicity), the mass estimate obtained using the “Summation method” is given by

$$M^S = \frac{-1}{4\pi G} \int_{\partial V} \left(\frac{\nabla P}{\rho} + (\mathbf{v} \cdot \nabla) \mathbf{v} \right) \cdot d\mathbf{S}, \quad (\text{A1})$$

where \mathbf{v} is the gas velocity on the infinitesimal surface element $d\mathbf{S}$, and ρ and P are the corresponding gas density and pressure. We can recover the true mass of the cluster if we measure \mathbf{v} , ρ and P of individual gas element and sum them up over the entire surface using Equation (A1). In reality, it is not possible to do so since observations are limited by finite spatial resolution of the instrument and we cannot measure the physical quantities of each individual gas element. In practice, we measure spatially averaged values above some resolution scale. In this spirit, we can spatially average Equation (A1) over the surface ∂V to arrive at a cluster mass estimate that is based on spatially averages of gas velocity, density and pressure. The mass obtained using this “Averaging method” is given by

$$M^A = \frac{-r^2}{G\langle\rho\rangle} \nabla\langle P\rangle + \frac{-r^2}{G\langle\rho\rangle} \nabla\langle\rho\rangle\sigma^2 + \frac{-r^2}{G} \langle(\mathbf{v})_\rho \cdot \nabla\rangle\langle\mathbf{v}\rangle_\rho, \quad (\text{A2})$$

where the angular bracket $\langle\cdots\rangle$ denotes spatial averaging, and $\langle\cdots\rangle_\rho$ denotes spatial averaging weighted by the gas density ρ over a spherical shell with radius r . This mass estimate M^A is the same as M^S , since mass is an extensive quantity and therefore it is not affected by any spatial averaging. Averaging of the nonlinear term $(\mathbf{v} \cdot \nabla) \mathbf{v}$ introduces to a new term in Equation (A2) that contains the density-weighted velocity dispersion tensor $\sigma_{ij}^2 \equiv \langle(v_i - \langle v_i \rangle_\rho)(v_j - \langle v_j \rangle_\rho)\rangle_\rho$. This term represents random motions of the gas elements internal to the resolution scale, which manifests as Doppler broadening in the emission lines. The bulk motion of the gas at the resolution scale is represented by $\langle\mathbf{v}\rangle_\rho$, which can be measured as Doppler shifts in the emission lines. Thus, using Equation (A2), we can recover cluster mass by accounting for the internal random motions and bulk motions from Doppler line broadening and shift, respectively. In the limit of large averaging scale, the motions within the volume are uncorrelated, and the random motion term dominates. At very small scale where we can resolve motions of individual gas elements, the motions consist solely of the bulk motion of the gas element and the random motion term is zero. While the breakdown of the motions into “bulk” and “random” components depends on the averaging scale, the recovered mass M^A from these gas motions is independent of the averaging scale. This can be understood by considering the fact that the Summation method is a limiting case of the Averaging method where the averaging scale approaches zero. Since both methods give the same mass estimates, the recovered mass from the Averaging method for any arbitrary averaging scale should give the same cluster mass as the Summation method. This means that as long as we measure both shifting and broadening of the emission line to account for both bulk and random gas motions, we can recover the cluster mass independent of the resolution scales of instruments.